A Magneto-Elastic Vector-Play Model Under Rotating Fields and Multiaxial Stress States

Luiz Guilherme da Silva[1,2,3], Laurent Bernard[3], Floran Martin[4], Anouar Belahcen[4], and Laurent Daniel[1,2]

[1]Université Paris-Saclay, CentraleSupélec, CNRS, Laboratoire de Génie Electrique et Electronique de Paris, 91192 Gif-sur-Yvette, France
[2]Sorbonne Université, CNRS, Laboratoire de Génie Electrique et Electronique de Paris, 75252 Paris, France
[3]GRUCAD/EEL/CTC, Federal University of Santa Catarina, Florianópolis 88040-900, Brazil
[4]Department of Electrical Engineering and Automation, Aalto University, 00076 Espoo, Finland

The hysteresis behavior of ferromagnetic materials under static stress is represented using an energy-based vector-play approach combined with a multiscale model. Using parameters identified from uniaxial measurements along one direction only, the modeling predictions agree well with the measured hysteresis loops of a non-oriented (NO) iron-silicon steel under multiaxial mechanical loadings and rotating fields. The hysteresis loss trend under stress is also reproduced with the proposed approach. Notably, the model reproduces the influence of complex mechanical loadings, such as shear, in the rotating losses description with errors lower than 12%.

***Index Terms*— 2-D magneto-mechanical loadings, magnetic hysteresis, magneto-elastic behavior, non-oriented (NO) iron-silicon.**

I. Introduction

IN ELECTRICAL devices, such as rotating machines or transformers, ferromagnetic materials may be submitted to mechanical stress and rotating magnetic fields in a complex multiaxial fashion, which can affect the efficiency and the operation of such machines [1], [2], [3]. Mechanical stress can originate from manufacturing processes, for instance, shrink fitting, or from the operation of high-speed devices, resulting in centrifugal forces, impacting the hysteresis and eddy current losses of electrical machines [4], [5], [6]. An energy-based vector-play approach [7] was recently proposed to model the coupled magneto-elastic behavior under static stress. This approach allows for modeling the magnetic hysteresis behavior under multiaxial magneto-elastic loadings. However, it has been validated under alternating magnetic fields only [8]. In this work, the vector-play model, with parameters identified from uniaxial tests along one direction only, is applied to represent the hysteresis behavior of a non-oriented (NO) Fe–Si under rotating fields and multiaxial stress loadings.

II. Modeling

A. Irreversible Behavior

In the energy-based vector-play model, the magnetic field $\vec{H}$ is defined as the sum of a reversible component $\vec{H}_{\text{rev}}$ and an irreversible component $\vec{H}_{\text{irr}}$. $\vec{H}_{\text{rev}}$ is directly related to a thermodynamic reversible state, while $\vec{H}_{\text{irr}}$ describes the dissipative effects in the magnetization process. An explicit solution for the energy-based model is proposed in [9]. The numerical implementation of the iterative model is performed considering a time discretization, divided into time steps, and starting from the demagnetized state. The reversible field $\vec{H}_{\text{rev}}$ is updated at each time step by

$$\vec{H}_{\text{rev}} = \begin{cases} \vec{H}_{\text{rev}(p)}, & \text{if } \left\| \vec{H} - \vec{H}_{\text{rev}(p)} \right\| \leq \kappa \\ \vec{H} - \kappa \frac{\vec{H} - \vec{H}_{\text{rev}(p)}}{\left\| \vec{H} - \vec{H}_{\text{rev}(p)} \right\|}, & \text{otherwise} \end{cases} \tag{1}$$

with $\vec{H}_{\text{rev}(p)}$ being the previous value of the reversible field. κ represents a pinning field and is equal to the coercive field in a hysteresis loop. To model the first magnetization curve and symmetric and asymmetric minor loops, a discrete distribution of pinning fields can be used [9]. In this case, the weight ω^k of each pinning field κ^k is introduced. It verifies

$$\sum_{k=1}^{N} \omega^k = 1 \tag{2}$$

with N representing the total number of pinning fields.

From experimental measurements, the influence of mechanical stress on the coercive field—and, therefore, on the pinning fields—is observed. A scaling of the pinning fields depending on the stress level is proposed in [7]

$$\kappa(\boldsymbol{\sigma}) = a\left(\sigma_{\text{eq}}\right)\kappa^k(\mathbf{0}) \quad \text{with } a\left(\sigma_{\text{eq}}\right) = \frac{H_c(\boldsymbol{\sigma})}{H_c(\mathbf{0})} \tag{3}$$

with the function $a(\sigma_{\text{eq}})$ being identified from uniaxial measurements of the coercive field H_c along rolling direction (RD), $\boldsymbol{\sigma}$ the second-order stress tensor, $\mathbf{0}$ the null second-order tensor, representing a stress-free situation, and σ_{eq} an equivalent stress proposed by [10]

$$\sigma_{\text{eq}} = \begin{cases} r - \sqrt{\vec{e}^{\,t}\left(r\boldsymbol{I} - \frac{3}{2}\boldsymbol{d}\right)^2\vec{e}}, & \text{if } \vec{e}^{\,t}\boldsymbol{d}\vec{e} \leq \dfrac{2r}{3} \\ r + \sqrt{\vec{e}^{\,t}\left(r\boldsymbol{I} - \frac{3}{2}\boldsymbol{d}\right)^2\vec{e}}, & \text{otherwise} \end{cases} \tag{4}$$

with r being a material parameter, identified from uniaxial measurements, which represents the stress value for which the

Manuscript received 8 June 2024; revised 15 August 2024; accepted 18 August 2024. Date of publication 27 August 2024; date of current version 26 November 2024. Corresponding author: L. G. da Silva (e-mail: luiz.dasilva@geeps.centralesupelec.fr).

Color versions of one or more figures in this article are available at https://doi.org/10.1109/TMAG.2024.3450651.

Digital Object Identifier 10.1109/TMAG.2024.3450651

magnetic permeability is maximum in an anhysteretic uniaxial configuration. $\vec{e}$ is the unit vector in the direction of the magnetic field $\vec{H}$, and $\vec{e}^{\,t}$ is its transpose. $\boldsymbol{d}$ is the deviatoric part of the stress tensor given by

$$\boldsymbol{d} = \boldsymbol{\sigma} - \frac{1}{3}\,\mathrm{tr}(\boldsymbol{\sigma})\boldsymbol{I} \tag{5}$$

with $\mathrm{tr}(\boldsymbol{\sigma})$ being the trace of the stress tensor.

The energy-based hysteresis model cannot reproduce the vanishing of hysteresis losses under rotating fields near the saturation [11]. To correct this drawback, mathematical approaches are inserted in the definition of the pinning field such that the losses description can be captured [11], [12]. Following a stress-free hysteresis case [12], [13], the pinning field is multiplied by a function f_1 defined as

$$\kappa^k\big(\vec{M},\boldsymbol{\sigma}\big) = f_1\big(\vec{M}\big)\,\kappa^k(\boldsymbol{\sigma}) \quad \text{with } f_1\big(\vec{M}\big) = 1 - \left(\frac{\|\vec{M}\|}{M_s}\right)^n \tag{6}$$

such that κ vanishes when the magnetization is close to the saturation. The parameter $n = 10$ is taken from [12] but could be used as an adjustable parameter.

B. Reversible Behavior

Neglecting dissipation, the energy-based approach reduces to a reversible process. A multiscale approach (MSM) models the reversible (anhysteretic) behavior. In this case, three scales are defined: the magnetic domain scale (denoted by the index α), the grain or single-crystal scale (denoted by the index g), and the representative volume element scale (RVE), in which the macroscopic constitutive laws are evaluated.

Considering homogeneous magnetic field and stress within the grains, the Gibbs free energy density at the domain scale is introduced and defined from its magnetic g_α^{mag}, magneto-elastic g_α^{el}, and anisotropy g_α^{an} parts, which are given by [14]

$$\begin{aligned} g_\alpha^{\mathrm{mag}} &= -\mu_0\,\vec{H}_{\mathrm{rev}}\cdot\vec{M}_\alpha \\ g_\alpha^{\mathrm{an}} &= K_1\big(\alpha_1^2\alpha_2^2+\alpha_1^2\alpha_3^2+\alpha_2^2\alpha_3^2\big) + K_2\big(\alpha_1^2\alpha_2^2\alpha_3^2\big) \\ g_\alpha^{\mathrm{el}} &= -\boldsymbol{\sigma} : \boldsymbol{\epsilon}_\alpha^{\mu} \end{aligned} \tag{7}$$

with $\vec{M}_\alpha$ representing the magnetization at the domain scale, defined by its direction $\vec{\alpha}$ and norm M_s, the saturation magnetization. K_1 and K_2 are the anisotropy constants. $\boldsymbol{\epsilon}_\alpha^{\mu}$ is the second-order magnetostriction strain tensor given by (for cubic symmetry)

$$\boldsymbol{\epsilon}_\alpha^{\mu} = \frac{3}{2}\begin{bmatrix} \lambda_{100}\big(\alpha_1^2-\frac{1}{3}\big) & \lambda_{111}\alpha_1\alpha_2 & \lambda_{111}\alpha_1\alpha_3 \\ \lambda_{111}\alpha_2\alpha_1 & \lambda_{100}\big(\alpha_2^2-\frac{1}{3}\big) & \lambda_{111}\alpha_2\alpha_3 \\ \lambda_{111}\alpha_3\alpha_1 & \lambda_{111}\alpha_3\alpha_2 & \lambda_{100}\big(\alpha_3^2-\frac{1}{3}\big) \end{bmatrix} \tag{8}$$

with components expressed in the grain coordinate system. The volume fraction p_α of a domain family with orientation $\vec{\alpha}$ is evaluated using a Boltzmann distribution [15]

$$p_\alpha = \frac{\exp\left(-A_s\ g_\alpha\right)}{\sum_\alpha \exp\left(-A_s\ g_\alpha\right)} \tag{9}$$

with A_s being a material parameter that can be identified from the initial susceptibility of a stress-free anhysteretic curve [14]. The magnetization $\vec{M}_g$ and magnetostriction strain $\boldsymbol{\epsilon}_g^{\mu}$ at the grain scale are then given by the corresponding volume averages

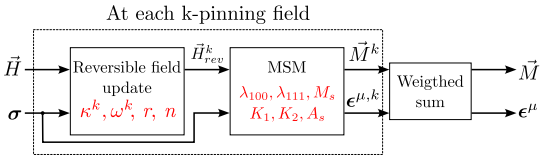

Fig. 1. Principle of the hysteresis model with material parameters indicated in red.

$$\vec{M}_g = \sum_\alpha p_\alpha \vec{M}_\alpha \quad \text{and } \boldsymbol{\epsilon}_g^{\mu} = \sum_\alpha p_\alpha \boldsymbol{\epsilon}_\alpha^{\mu}. \tag{10}$$

At the macroscopic scale, the magnetization $\vec{M}$ and magnetostriction strain $\boldsymbol{\epsilon}^{\mu}$ are given by the average behavior of each grain

$$\vec{M} = \sum_g p_g \vec{M}_g \quad \text{and } \boldsymbol{\epsilon}^{\mu} = \sum_g p_g \boldsymbol{\epsilon}_g^{\mu} \tag{11}$$

where p_g represents the volume fraction of each grain orientation used to describe the crystallographic texture [8].

In this work, only static mechanical loadings are considered, and dissipation is defined through variations in the magnetic field. The hysteresis model under variable fields and constant stress is summarized in Fig. 1.

The magnetization and magnetostriction strain for each pinning field are written as $\vec{M}^k(\vec{H}^k_{\mathrm{rev}},\boldsymbol{\sigma})$ and $\boldsymbol{\epsilon}^{\mu,k}(\vec{H}^k_{\mathrm{rev}},\boldsymbol{\sigma})$. By using a weighted sum, the total magnetization and magnetostriction strain are given by

$$\vec{M} = \sum_{k=1}^{N} \omega^k \vec{M}^k\big(\vec{H}^k_{\mathrm{rev}},\boldsymbol{\sigma}\big) \quad \text{and } \boldsymbol{\epsilon}^{\mu} = \sum_{k=1}^{N} \omega^k \boldsymbol{\epsilon}^{\mu,k}\big(\vec{H}^k_{\mathrm{rev}},\boldsymbol{\sigma}\big). \tag{12}$$

III. Identification of Material Parameters

The material tested in this work is an NO Fe–Si whose crystallographic texture measurements are reported in [8]. The geometry of the sample, adapted to the single-sheet biaxial setup, consists of six legs with a measurement area of 20 × 20 mm^2. The magnetic field and induction are measured with an H-coil and a B-coil, respectively. The magnetic induction is controlled at 10 Hz in the hysteresis measurements. Much more details about the experimental setup are presented in [16] and [17]. The material parameters are identified from uniaxial measurements performed along RD [8]. The set of experimental data used for parameter identification includes a stress-free anhysteretic curve, 12 stress-free symmetric hysteresis loops, such that a coercive field characteristic versus peak magnetic field can be defined, and three major hysteresis loops under uniaxial stress, which allow capturing a stress-dependent pinning field (in the range of −50 to +100 MPa). The anhysteretic parameters are listed in Table I. The hysteresis parameters ω^k and κ^k are also given in [8] considering $N = 25$ pinning fields. The parameter r, related to the equivalent stress, is $r = 20$ MPa.

TABLE I

PARAMETERS OF THE REVERSIBLE MODELING [8]

M_s (A/m)	λ_{100} (ppm)	λ_{111} (ppm)	K_1 (kJ/m^3)	K_2 (kJ/m^3)	A_s (m^3/J)	r (MPa)
$1.4\,10^6$	11.5	−4.5	38	0	$1.1\,10^{-2}$	20

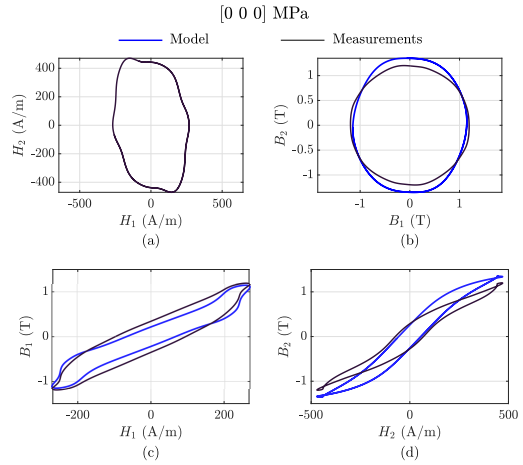

Fig. 2. Stress-free magnetic behavior. Comparison between measurements [16] and the proposed modeling. (a) Magnetic field loci. (b) Induction loci. (c) Hysteresis behavior along RD under rotating field. (d) Hysteresis behavior along TD under rotating field.

IV. VALIDATION

The measurements were performed considering in-plane stress assumption and controlling the induction [16]. The 2-D-stress tensor is denoted as $[\sigma_{11}\ \sigma_{22}\ \sigma_{12}]$ with 1 representing RD and 2 transverse direction (TD). Using the measured waveform of the magnetic field as input of the model [see Fig. 2(a)], the model reproduces the measured loci of induction, as shown in Fig. 2(b). The hysteresis loops for RD and TD are presented in Fig. 2(c) and (d), showing that the modeling results capture the general behavior of the hysteresis loops. Main differences, also noted in the induction loci, are observed in Fig. 2(d), in which the model overestimates the induction at high fields along TD. This difference can be attributed to a limitation in which the anisotropy is underestimated in modeling, as discussed in [8]. Anisotropy is indeed accounted for through the crystallographic texture information but is not considered in the hysteresis parameters that are identified from measurements along RD only.

The influence of the function $f_1(\vec{M})$ in defining the pinning field can be observed in the modeled rotating losses curve. The measured losses are shown in Fig. 3 for the stress-free case. It can be noted that above 1.3 T, the decrease in hysteresis losses is insured using this adaptation. This result is an improvement compared to the approach presented in [8], which results in the solid line shown in Fig. 3. Due to the limitations of the experimental setup, the maximum measured induction amplitude is 1.2 T. If tests under higher induction levels were available, the n-parameter can be adequately identified so that the modeling results can be adjusted to the measurements.

Under a compression of 30 MPa applied along RD, the measured magnetic field waveforms shown in Fig. 4(a) are inserted in the model. The induction loci presented in Fig. 4(b) shows that the model reproduces the measured behavior. A better matching is observed at high induction levels.

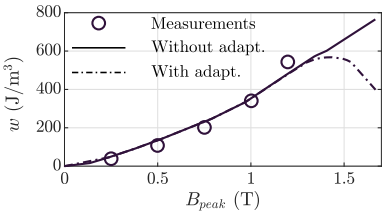

Fig. 3. Stress-free hysteresis losses. Comparison between the measurements (markers) [16] and the model without pinning field adaption (solid line) [8] and with the adaption (dashed line).

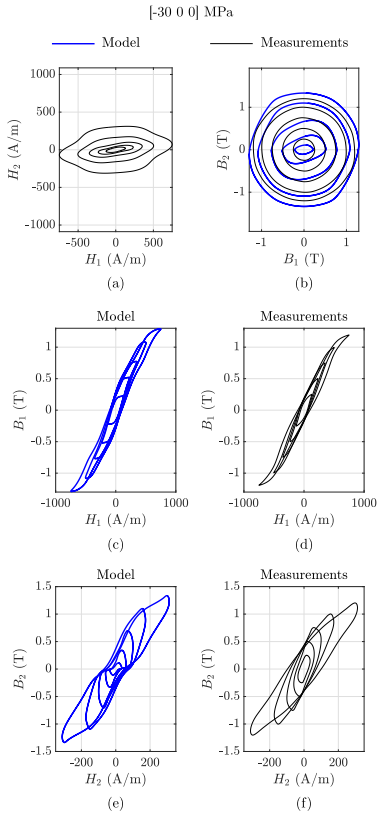

Fig. 4. Magnetic behavior under compression applied along RD. Comparison between measurements [16] and the proposed modeling. (a) Magnetic field loci. (b) Induction loci. (c) Modeled hysteresis behavior along RD under rotating field. (d) Measured hysteresis behavior along RD under rotating field. (e) Modeled hysteresis behavior along TD under rotating field. (f) Measured hysteresis behavior along TD under rotating field.

The magnetic hysteresis response along RD is satisfactorily reproduced in modeling [see Fig. 4(c) and (d)]. Along TD, the modeled loops differ more significantly from measurements [see Fig. 4(e) and (f)], which is also observed in the induction loci of Fig. 4(b). As for the stress-free case, the differences are highlighted particularly for low induction levels. By increasing the induction, the material gets closer to saturation, and anisotropy effects are less significant so that the modeled induction loci are closer to the measured circle.

In a challenging magneto-elastic configuration, shear stress is applied together with a rotating field, as shown in Fig. 5(a). Despite the complex hysteresis loop shape, the modeling components B_1 and B_2 are close to the measurements, as observed in Fig. 5(c) and (d). As previously discussed, the model overestimates the induction along TD, as also seen in the induction loci of Fig. 5(b). Another limitation under this magneto-elastic configuration is noted in the region of $B_2 = 0$ along TD [see Fig. 5(d)]. This disparity between modeling

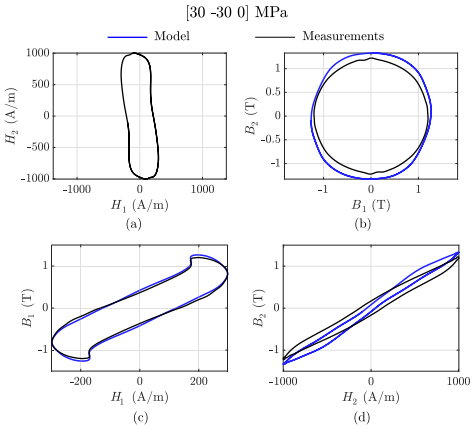

Fig. 5. Magnetic behavior under shear. Comparison between measurements [16] and the proposed modeling.

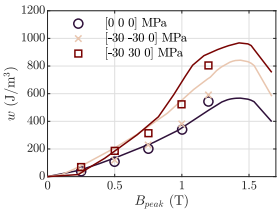

Fig. 6. Comparison between measured [16] (markers) and modeled (solid lines) hysteresis losses under rotating field and static multiaxial stress.

and measurements results in a difference of about 12% in the rotating hysteresis losses. Using different pinning fields for RD and TD, as presented in [18], could improve the modeling results. However, in addition to uniaxial measurements along RD, experimental results along TD would be required to identify the pinning fields.

The model captures the trend of hysteresis losses under biaxial stress and rotating field, as observed in Fig. 6. Notably, the increase in hysteresis losses, especially under shear, is represented in the approach. By adapting the pinning field (6), the model represents the vanishing of hysteresis losses in the region of domain rotation for different mechanical states.

V. Conclusion

Using material parameters identified from uniaxial tests along one direction only, the combination of a vector-play model and an MSM predicts the magnetic hysteresis loops and the loss trend of a ferromagnetic material under rotating fields and multiaxial mechanical loadings. The model validation has been performed by considering complex magneto-elastic loadings different from those used for parameter identification. To improve the description of stress-induced anisotropy effects, the heterogeneity of the mechanical loading at the grain scale could be taken into account from an MSM using localization and homogenization schemes. Future works include the numerical inversion of the model to be plugged into a B-conform finite element simulation in order to evaluate the influence of mechanical loadings on the efficiency of electromagnetic devices.

Acknowledgment

This work was supported in part by the Brazilian Federal Agency for Support and Evaluation of Postgraduate Education (CAPES) and in part by the French Committee for the Evaluation of University and Scientific Cooperation with Brazil (COFECUB) under Project 88881.191763/2018-01. The work of Laurent Bernard was supported by the National Council for Scientific and Technological Development, Brazil — CNPq. The work of Floran Martin and Anouar Belahcen was supported by the Research Council of Finland through the Centre of Excellence in High-Speed Electromechanical Energy Conversion Systems under Grant 346438.

References

[1] Y. Guo, J. Guo Zhu, J. Zhong, H. Lu, and J. X. Jin, "Measurement and modeling of rotational core losses of soft magnetic materials used in electrical machines: A review," *IEEE Trans. Magn.*, vol. 44, no. 2, pp. 279–291, Feb. 2008.

[2] K. Yamazaki and H. Takeuchi, "Impact of mechanical stress on characteristics of interior permanent magnet synchronous motors," *IEEE Trans. Ind. Appl.*, vol. 53, no. 2, pp. 963–970, Mar. 2017.

[3] Z. Zhang, A. Nysveen, B. J. Fagemyr, A. Chen, H. Ehya, and R. Nilssen, "Material characterization and stator core loss computation of synchronous generators with stacking force accounted," *IEEE Trans. Ind. Appl.*, vol. 60, no. 1, pp. 239–248, Jan./Feb. 2024.

[4] K. Ali, K. Atallah, and D. Howe, "Prediction of mechanical stress effects on the iron loss in electrical machines," *J. Appl. Phys.*, vol. 81, no. 8, pp. 4119–4121, Apr. 1997.

[5] K. Fujisaki et al., "Motor core iron loss analysis evaluating shrink fitting and stamping by finite-element method," *IEEE Trans. Magn.*, vol. 43, no. 5, pp. 1950–1954, May 2007.

[6] K. Yamazaki and W. Fukushima, "Loss analysis of induction motors by considering shrink fitting of stator housings," *IEEE Trans. Magn.*, vol. 51, no. 3, pp. 1–4, Mar. 2015.

[7] L. G. D. Silva, A. Abderahmane, M. Domenjoud, L. Bernard, and L. Daniel, "An extension of the vector-play model to the case of magneto-elastic loadings," *IEEE Access*, vol. 10, pp. 126674–126686, 2022.

[8] L. G. da Silva, L. Bernard, F. Martin, A. Belahcen, and L. Daniel, "Multiaxial validation of a magneto-elastic vector-play model," *IEEE Trans. Magn.*, vol. 59, no. 11, pp. 1–10, Nov. 2023.

[9] F. Henrotte, A. Nicolet, and K. Hameyer, "An energy-based vector hysteresis model for ferromagnetic materials," *COMPEL-Int. J. Comput. Math. Elect. Electron. Eng.*, vol. 25, pp. 71–80, Jan. 2006.

[10] P. Rasilo, U. Aydin, F. Martin, A. Belahcen, R. Kouhia, and L. Daniel, "Equivalent strain and stress models for the effect of mechanical loading on the permeability of ferromagnetic materials," *IEEE Trans. Magn.*, vol. 55, no. 6, pp. 1–4, Jun. 2019.

[11] A. Bergqvist, "Magnetic vector hysteresis model with dry friction-like pinning," *Phys. B, Condens. Matter*, vol. 233, no. 4, pp. 342–347, Jun. 1997.

[12] A. Sauseng, L. Domenig, K. Roppert, and M. Kaltenbacher, "Adaptions of the energy-based hysteresis model for correct rotational losses," in *Proc. IEEE 20th Biennial Conf. Electromagn. Field Comput. (CEFC)*, Oct. 2022, pp. 1–2.

[13] A. Sauseng, M. Kaltenbacher, and K. Roppert, "Revisiting the dry friction-like magnetic vector hysteresis model," *J. Magn. Magn. Mater.*, vol. 604, Aug. 2024, Art. no. 172285.

[14] L. Daniel, O. Hubert, N. Buiron, and R. Billardon, "Reversible magneto-elastic behavior: A multiscale approach," *J. Mech. Phys. Solids*, vol. 56, no. 3, pp. 1018–1042, Mar. 2008.

[15] N. Buiron, L. Hirsinger, and R. Billardon, "A multiscale model for magneto-elastic couplings," *Le J. de Physique*, vol. 9, pp. 187–196, Sep. 1999.

[16] U. Aydin et al., "Effect of multi-axial stress on iron losses of electrical steel sheets," *J. Magn. Magn. Mater.*, vol. 469, pp. 19–27, Jan. 2019.

[17] U. Aydin et al., "Rotational single sheet tester for multiaxial magneto-mechanical effects in steel sheets," *IEEE Trans. Magn.*, vol. 55, no. 3, pp. 1–10, Mar. 2019.

[18] L. Prigozhin, V. Sokolovsky, J. W. Barrett, and S. E. Zirka, "On the energy-based variational model for vector magnetic hysteresis," *IEEE Trans. Magn.*, vol. 52, no. 12, pp. 1–11, Dec. 2016.